Magnetotransport study of van der Waals $CrPS_4$/(Pt, Pd) heterostructures: Spin-flop transition and room-temperature anomalous Hall effect

Rui Wu[1,2,3], Andrew Ross[1,4], Shilei Ding[1,5], Yuxuan Peng[5], Fangge He[1], Yi Ren[3], Romain Lebrun[1,4], Yong Wu[1,6], Zhen Wang[1,7], Jinbo Yang[5], Arne Brataas[2,*], Mathias Kläui[1,2,*]

1. Institute of Physics, Johannes Gutenberg-University Mainz, Staudingerweg 7, Mainz 55128, Germany

2. Center for Quantum Spintronics, Norwegian University of Science and Technology, Trondheim 7491, Norway

3. Beijing Academy of Quantum Information Sciences, Beijing, 100193, P. R. China

4. Unité Mixte de Physique, CNRS, Thales, Université Paris-Saclay, Palaiseau, 91767, France.

5. State Key Laboratory for Mesoscopic Physics, School of Physics, Peking University, Beijing 100871, China

6. School of Materials Science and Engineering, University of Science and Technology Beijing, Beijing 100083, China

7. Department of Applied Physics, Chang'an University, Xi'an 710064, China

*Corresponding authors: arne.brataas@ntnu.no; klaeui@uni-mainz.de

Abstract

We study magneto-transport in heterostructures composed of the van der Waals antiferromagnet $CrPS_4$ and the heavy metals Pt and Pd. In both devices, the transverse resistance (R_{xy}) signal reveals the spin-flop transition of $CrPS_4$ and a strong anomalous Hall effect at temperatures up to 300 K. While $CrPS_4$/Pt devices allow for easy detection of the spin-flop transition, $CrPS_4$/Pd devices show a more substantial enhancement in anomalous Hall effect at temperatures above 70 K and exhibit a topological Hall effect

signal, possibly related to chiral spin structures at the interface. The longitudinal magnetoresistance (R_{xx}) results from a combination of spin-Hall magnetoresistance and the negative magnetoresistance that can be explained by a field-induced change of the electronic band structure of $CrPS_4$.

Introduction

The coupling between spin and orbital degrees of freedom in materials, especially in heavy metals such as Pt, Pd and W, and in topological insulators, has led to new directions in spintronics, such as spin-orbitronics[1-3]. In metals with significant spin-orbit coupling, the spin Hall effect (SHE)[4] generates a spin current from a charge current that in turn interacts with adjacent magnetic materials[5]. Spin-orbit coupling has opened a new route to detect and manipulate the magnetic properties of magnetic materials. For example, the spin-Hall magnetoresistance (SMR)[5], originating from the interaction of the spin currents generated by the heavy metals and the magnetic layer that can be described as a nonequilibrium proximity effect, is a useful tool to probe the magnetic moments of the magnetic materials. The SMR is especially important in magnetic insulators, where a direct measurement with electric currents flowing in the magnetic layer is not possible.

At present, with the requirements of device miniaturization and low power consumption, the research on 2-dimensional (2D) spintronics/magnonics devices based on Van der Waals (vdW) magnets with reduced dimensionality, high flexibility, and tunability is attracting considerable attention[6-12]. Especially, despite the Mermin-Wagner theorem[13], the long-range magnetic ordering is maintained even at the monolayer scale in many vdW magnets because of the sizeable magnetic anisotropy, which enables potential applications of these materials at the 2D limit. There have been observations of a large tunneling magnetoresistance [14,15], long-range magnon transport[16,17], the electric control of magnetism[18,19] in the vdW magnets. All these properties are preferred in the spintronic/magnonics devices.

The CrX_3 (X = I, Cl, Br) series is an example of typical vdW magnets. The thin bulk flake materials have A-type antiferromagnetic ordering so that the magnetic moments within each layer are parallel as in ferromagnets, while the inter-layer coupling is antiferromagnetic[20]. Furthermore, the antiferromagnetic coupling between layers causes the magnetic properties to differ for odd and even numbers of stacking layers[20,21]. The large tunneling magnetoresistance effect and controllability of magnetism with both electric and mechanic stimuli have been demonstrated in these materials, making them appealing for spintronics devices[14,15,19,21]. However, the CrX_3 class of materials is unstable in both air and light, limiting their easy application in practical devices.

A more robust alternative is the thiophosphate ($CrPS_4$) that also belongs to the A-type antiferromagnet family and has a layered structure with vdW interlayer interactions, where spins within each monolayer are aligned ferromagnetically out-of-plane, as schematically shown in FIG. 1(a)[22,23]. Both density functional theory (DFT) calculations [24] and experimental results[25] have indicated that single-layer $CrPS_4$ is a 2-dimensional ferromagnet. Compared with some members of the CrX_3 series, $CrPS_4$ is air-stable and has a sizeable Néel temperature (T_N=36 K)[26]. A T_C = 25 K is observed in single-layer $CrPS_4$, which is smaller than the bulk T_N[25]. In addition, $CrPS_4$ exhibits a spin-flop (SF) transition, where the Néel vector **n** is rotated by the external magnetic field **H** from **n**//**H** to $\mathbf{n}\perp\mathbf{H}$ configurations. The SF can minimize the effective anisotropic energy that the spin experiences and allows for tuning of the effective anisotropy, for instance crucial for realizing devices based on the long-distance spin transport in antiferromagnetic materials in the superfluid or diffusion regimes[16,17,27-29]. Moreover, the SF field is H_{sf} = 0.9 T at 5 K for bulk $CrPS_4$[26], which is relatively accessible compared to other antiferromagnetic systems with a H_{sf} of several Tesla or tens of Tesla[26,30,31]. For application, electrical detection of the antiferromagnetic order is key. However, the electrical readout of $CrPS_4$ has not been reported to date, calling for the identification of magnetoresistance effects that lend themselves to electrical detection of the magnetic order.

In this paper, we report measurements of magneto-transport in $CrPS_4$/heavy metal (Pt, Pd) heterostructures. The Hall effect measurement reveals the SF transition， indicating a spin transparent vdW/heavy metal interface. Moreover, we measure a persistence of the anomalous Hall effect (AHE) in the heterostructures at temperatures above the T_N of the bulk $CrPS_4$, and up to 300 K. Especially, we report a topological Hall effect (THE) in the high-temperature range up to 240 K in the device with Pd but not in the device with Pt, that can be explained by a smaller Dzyaloshinskii–Moriya interaction (DMI) at the vdW/heavy metal interface in the Pt based devices possibly related to the different Pt and Pd work functions. Furthermore, for a Pd based heterostructure, the field dependence of the longitudinal resistance shows a strong ferromagnetic-like signal at temperatures up to 300 K as well as a strong negative magnetoresistance at temperatures below T_N, possibly related to the electronic band structure change in $CrPS_4$ induced by the external magnetic field. The angular dependence of longitudinal resistance confirms the ferromagnetic ordering above the bulk T_N of $CrPS_4$ and shows a signature of the SF at temperatures below T_N.

Results and discussion

The $CrPS_4$ flakes are mechanically exfoliated from $CrPS_4$ single crystals with adhesive tape and transferred to an α-Al_2O_3(0001) substrate. The peak positions of Raman spectroscopy are consistent with the bulk $CrPS_4$[25,32], which indicates the $CrPS_4$ flake is in good condition without significant surface degradation (see supplementary FIG. S1)[33]. An atomic force microscopy image of a typical flake is shown in FIG. 1(b). The profile across the flake edge indicates that its thickness is about 40 nm. To maintain a clean interface, we complete the entire process in a glove box directly connected to a Molecular-beam epitaxy (MBE) deposition system. Next, we transfer the substrates with $CrPS_4$ flakes to the MBE without exposure to air. During the metal deposition process, the substrate is cooled to about 90 K by liquid nitrogen to reduce any damage to the $CrPS_4$ surface during the deposition process. The deposition rate is 1 nm/min. A reference $CrPS_4$/Pd sample with Pd deposited using magnetron sputtering at room temperature also without exposure to air does not significantly alter the transport properties. Thus, we prepared the $CrPS_4$/Pt sample by magnetron sputtering, exfoliating the flakes in a load-lock chamber connected to the main sputtering chamber in a vacuum of about 5×10^{-6} mbar. The thickness of the heavy metal layers is about 10 nm. Finally, we obtained Hall devices illustrated in FIG. 1(c) by photolithography and ion beam etching. To obtain better conductivity at the edge of the sheet, we deposited 60 nm thick Au contacts to cover the flake's edge, as shown in FIG. 1(d).

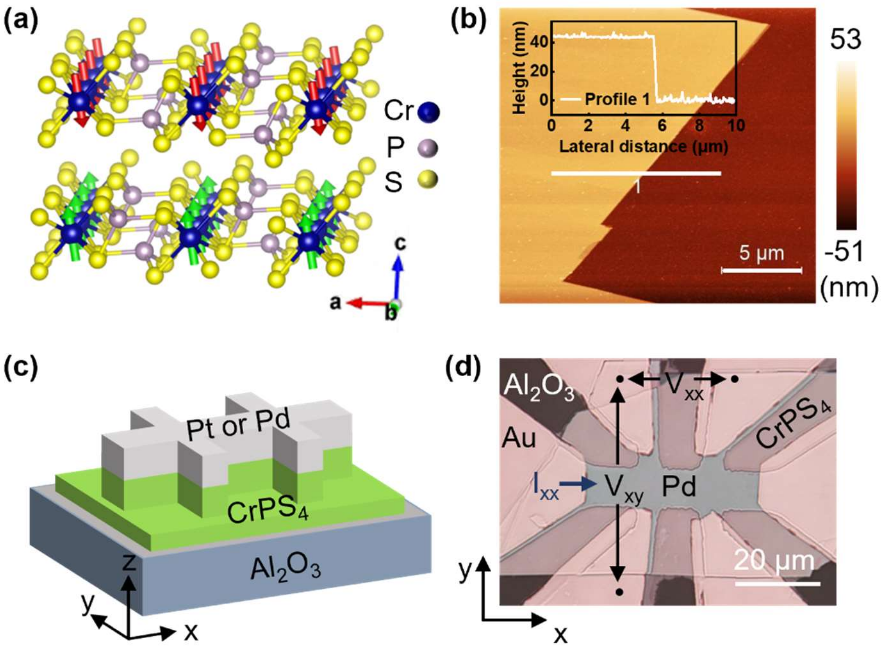

FIG. 1. (a) Crystalline and magnetic structures of $CrPS_4$. (b) Atomic force microscopy

image of a $CrPS_4$ flake with a thickness of about 40 nm. The inset shows the profile across the flake edge. (c) Schematic of the $CrPS_4$/(Pt, Pd) device. (d) Optical microscope image of a $CrPS_4$/Pd device.

We first studied the transport in the Hall geometry of the $CrPS_4$/(Pt, Pd) devices. With the magnetic field applied in the out-of-plane direction (z-axis) and a constant current I_{xx}=1 mA applied along the longitudinal channel, the V_{xy} was measured while varying the magnetic field and external temperature and shown in FIG. 1(d). Considering that the width of the current channel in the Hall bar is about 9 μm, the current density **J** is about 1.1×10^{6} A/cm^{2}. The transverse resistance is defined as $R_{xy} = V_{xy}/I_{xx}$. We have subtracted a linear background for the R_{xy} signal due to the normal Hall effect of Pt and Pd (see supplementary FIG. S2).

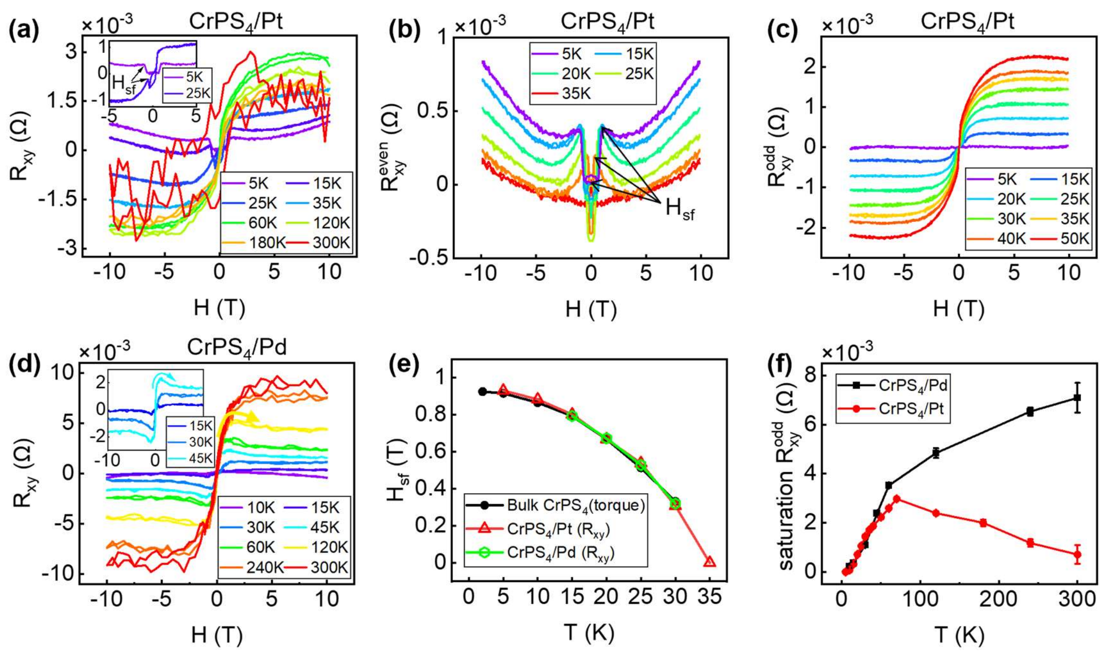

FIG. 2. (a) R_{xy} signal of $CrPS_4$/Pt device measured at different temperatures, and the inset shows the zoomed-in curves obtained at 5 K and 25 K. (b) The even component (R_{xy}^{even}) odd component (R_{xy}^{odd}) of R_{xy} of the $CrPS_4$/Pt device are presented. (d) The R_{xy} of $CrPS_4$/Pd device measured at different temperatures, and the inset shows the

zoomed-in curves obtained at 15 K, 30 K, and 45 K. (e) The SF fields obtained from $CrPS_4$/Pt (red triangle) and $CrPS_4$/Pd (blue diamond) devices in comparison with values from the bulk $CrPS_4$ (black sphere, data adapted from Ref. [17]). (f) The comparison of the saturation of the R_{xy}^{odd} versus temperature plots for the $CrPS_4$/Pd (black square) and $CrPS_4$/Pt (red circle) devices.

As shown in FIG. 2(a), there are two central features in the R_{xy} curves of the $CrPS_4$/Pt device. Firstly, at temperatures $T < T_N$, the R_{xy} curves show significant jumps at a field H_{sf}, and they are asymmetric as a function of magnetic field, see the inset of FIG. 2(a). This feature has, to the best of our knowledge, not been seen in other magnetic systems and we next check if it is related to the SF of the $CrPS_4$. In order to separate the possible SF signal from the aforementioned AHE, which should be symmetric, we separate R_{xy} into an even component and an odd component, i.e. $R_{xy}(H) = R_{xy}^{even}(H) + R_{xy}^{odd}(H)$, where

$$R_{xy}^{odd}(H) = \frac{R_{xy}(H)-R_{xy}(-H)}{2},$$

$$R_{xy}^{even}(H) = \frac{R_{xy}(H)+R_{xy}(-H)}{2}.$$

FIG. 2(b) and 2(c) show $R_{xy}^{even}(H)$ and $R_{xy}^{odd}(H)$ at different temperatures. It is found that the jumps in the R_{xy} curves are only observed in R_{xy}^{even} signal at temperature below T_N. The slow increase of R_{xy}^{even} at higher fields is likely caused by a small contribution from the longitudinal resistance R_{xx} due to the small (inevitable) offset of the V_{xy} contacts[34]. Finally, we now plot the positions of the jumps as a function of the temperature in FIG. 2(e). The position of the jumps agrees extremely well with the SF field H_{sf} in the bulk $CrPS_4$ obtained from torque measurements[23], as compared in FIG. 2(f). When the temperature is close to T_N, the jumps tend to overlap with each other (see the results for T=35 K in FIG. 2(b)). Thus, this shows that we can detect the spin-flop electrically in this system as a key step for electrical read-out.

Secondly, as shown in FIG. 2(a), the amplitude of R_{xy} shows a non-monotonic temperature dependance. This feature is majorly reflected in the R_{xy}^{odd} signal as shown in FIG. 2(c). The saturation R_{xy}^{odd} monotonically increases with increasing temperature when T < 70 K and then decreases when T > 70 K, as shown in FIG. 2(f). It is found that a non-zero R_{xy}^{odd} can be found even at room temperature, far above the bulk T_N. This behavior contrasts with the usual situation where R_{xy} due to the AHE in ferromagnetic thin films decreases with the increase of the temperature and disappears at the Curie temperature (T_C)[35]. It is noted that no AHE observed in the Hall bar of pure heavy metals (Pt or Pd) in our experiment, the observed ferromagnetic-like signal of the $CrPS_4$/Pt at above T_N is ascribed to the enhanced ordering temperature of the interface $CrPS_4$ layer in contact with Pt and with an enhanced spin-orbit coupling[36]. The enhancement of magnetic ordering temperature has been observed in several vdW/heavy metal heterostructures, including the $Cr_2Ge_2Te_6$/W and $Cr_2Ge_2Te_6$/Ta systems, due to the proximity effect from the heavy metals[37]. As we know, the bulk $CrPS_4$ has a layered structure and a weak interlayer exchange coupling. When $T > T_N$, the bulk $CrPS_4$ becomes paramagnetic while the interface $CrPS_4$ can stay ferromagnetic because the extended 5d orbitals of heavy metals with strong SOC can participate in the reconstructed orbital hybridization in the adjacent $CrPS_4$ layer and promote the intralayer exchange interaction[37]. The different temperature dependence below and above 70 K is from the competition of thermally enhanced charge transfer between Pt and $CrPS_4$, which enhances the magnetic ordering, and the ferromagnetic to paramagnetic transition induced by increasing the temperature. It should be noted that the poor signal to noise at 300 K results from the poor temperature stability at high temperatures compared to lower temperatures. This is because the cryostat has a variable temperature insert that is optimized for temperatures of 200 K or below.

As shown in the FIG. 2(d), the main features of the R_{xy} signal are also observed in the $CrPS_4$/Pd sample. Firstly, when $T < T_N$, the asymmetry and jumps in the R_{xy} curves is also present in $CrPS_4$/Pd device, as shown in the inset of FIG. 2(d) (see also supplementary FIG. S3(a)). The R_{xy}^{even} and R_{xy}^{odd} are calculated and given in supplementary FIG. S3(b-c), respectively. The jumps in the R_{xy} are clearly visible in the $R_{xy}^{even}(H)$ signal in a narrow temperature range of 15 K-30 K (see supplementary FIG. S3(a)). The position of the jumps again agrees extremely well with the H_{sf} obtained from the torque measurement of the bulk $CrPS_4$[23], as compared in FIG. 2(e), confirming that the mechanism for the jumps in the R_{xy} curves is the SF transition in the $CrPS_4$ flake thus showing that again we can realize electrical read-out.

Secondly, the R_{xy} signal of the $CrPS_4$/Pd sample shows a steady increase with increasing temperature, even above the T_N of bulk $CrPS_4$. The difference between these two samples is that the amplitude of R_{xy} of the $CrPS_4$/Pd sample does not reach its maximum even when the temperature is above room temperature as shown in FIG. 2(f), while it reaches the maximum at 70 K in the $CrPS_4$/Pt sample. When the temperature is lower than T_N of bulk $CrPS_4$, the two curves almost completely overlap. But when the temperature is higher than T_N, they start to diverge, and show a completely different temperature-dependent trend above 70 K. The decrease of the AHE in $CrPS_4$/Pt sample is ascribed to the thermal activation of spin excitations at higher temperatures. In the $CrPS_4$/Pd sample, the increase of AHE is slowed down by the thermal effect and the opposite trend is not observed in the temperature range studied. The difference between those two heterostructures can be possibly ascribed to the different electronic properties of the two heavy metals, e.g., the larger work function of Pt ($\Phi_{\mathrm{Pt,vac}} = 5.65\ eV$) compared to Pd ($\Phi_{\mathrm{Pd,vac}} = 5.12\ eV$)[38] can make the charge transfer process at the $CrPS_4$/Pd interface much easier than that at the $CrPS_4$/Pt interface and give a more prominent T_C enhancement in $CrPS_4$.

Thirdly, we observe a non-monotonic field dependence in some R_{xy} curves of the $CrPS_4$/Pd device (see supplementary FIG. S3(a) and the inset in FIG. 2(d)), i.e., when the magnetic field is larger than a particular value, the Hall coefficient R_{xy} drops anomalously and presents a peak in the curve. This behavior becomes visible at 25 K and stronger between 60 K and 120 K before vanishing at 180 K (see the inset in supplementary FIG. S3(c)). It is reminiscent of signals resulting from a topological Hall effect (THE) [39-41] and usually associated with topological chiral magnetic structures, such as skyrmions and chiral domain walls[42,43]. These are stabilized by interfaces with DMI, which can be introduced in the ultrathin ferromagnetic layer adjacent to a heavy metal layer due to strong spin-orbit coupling and broken inversion symmetry[43]. The thermal fluctuations have been demonstrated to play a key role in the formation of topological spin textures in Cr_2O_3/Pt heterostructure, where a THE was observed at 345 K, higher than the T_N of Cr_2O_3 (~307 K)[44]. The THE in the $CrPS_4$/Pd device at above T_N could result from the same mechanisms. However, the THE is not observed in the $CrPS_4$/Pt device, as shown in FIG. 2(a) and 2(b). This absence might arise from different DMI strength at the interfaces in two systems since the DMI is also correlated with the work functions of the heavy metals[45].

Although the SF transition in the R_{xy} signal has been reported in the CoO(001)/Pt system[46], some other systems also show SF transition in the R_{xx} signal, such as CrI_3/Pt [47] and α-Fe_2O_3/Pt[48] systems. Different spin dynamics could yield different behaviors in SMR during the SF transition, considering that the transverse SMR signal is proportional to the in-plane Néel vector components $n_x \cdot n_y$, while the longitudinal signal is proportional to $n_y \cdot n_y$[5,49], with the coordinate system defined in FIG. 2(c) and 2(e).

We next study the field and angular dependance of longitudinal transport properties of the $CrPS_4$/Pd sample to compare this with the transverse signals. For the field dependence, the longitudinal magnetoresistance is defined as $MR_{xx} = \frac{[R_{xx}(H)-R_{xx}(H=0)]}{R_{xx}(H=0)}$, where the longitudinal resistances $R_{xx} = \frac{V_{xx}}{I_{xx}}$, and the current I_{xx} has the same value as in the Hall measurement. Since Pd exhibits a significant Hanle-induced MR_{xx}[50], we obtain a signature of $CrPS_4$ in FIG. 3 by subtracting the signal of a control Pd device from the signal of the $CrPS_4$/Pd device, i.e., $\delta MR_{xx} = MR_{xx}(\mathrm{CrPS_4/Pd}) - MR_{xx}(\mathrm{Pd})$ (see supplementary FIG. S4).

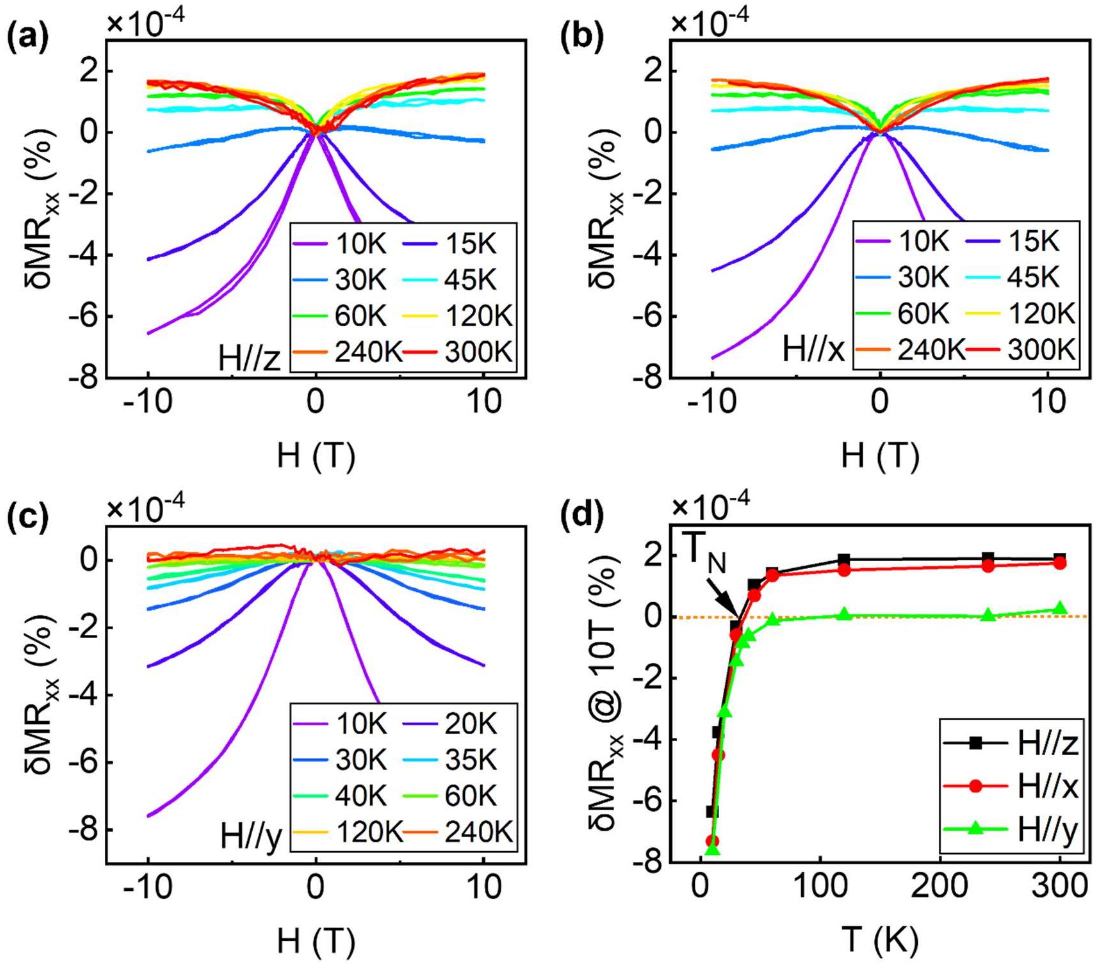

FIG. 3. (a-c) The longitudinal magnetoresistance δMR_{xx} of the $CrPS_4$/Pd device, as a function of magnetic field applied along z, x, and y axes, respectively. (d) The

corresponding saturation δMR_{xx} (at 10 T) versus temperature.

FIG. 3(a) shows the δMR_{xx} of the $CrPS_4$/Pd sample measured at different temperatures with the magnetic field applied along z axis. The δMR_{xx} is negative when the temperature is lower than T_N, while it is positive at temperatures above T_N and remains observable even at 300 K, which is of importance for possible room temperature devices. As shown in FIG. 3(b), a nearly similar δMR_{xx} behavior was observed with the magnetic field applied along x axis. However, when the field was applied along the x axis, the positive δMR_{xx} disappears at temperature above T_N, while the negative δMR_{xx} below T_N still exists, as shown in FIG. 3(c). These behaviors can also be seen in the plot of nominal saturation δMR_{xx} (at 10 T) versus temperature (FIG. 3(d)), where a sharp change at $T<T_N$ and a saturation above 60 K can be seen in all three directions. The significant negative δMR_{xx} was found only below T_N of $CrPS_4$. Thus, this must be related to the electronic structure change in the $CrPS_4$ correlated with a magnetic structure transition from antiferromagnetic to ferromagnetic (i.e. the spin-flip process) induced by the magnetic field. The positive magnetoresistance at temperature much higher than the T_N was observed, which is likely due to the SMR effect from the $CrPS_4$/Pd interface with possible enhanced order temperature of the top $CrPS_4$ layer. Furthermore, the R_{xy} signal obtained in the H//x and H//y configurations shows some features related to the spin-flip and magnetic ordering transitions of the bulk $CrPS_4$, respectively (see supplementary FIG. S5(a-b)). This again demonstrates the transparency of the vdW/heavy metal interface in those samples.

In order to better understand the conjecture observed in the δMR_{xx} signal at $T<T_N$, the DFT calculation of the electronic structures of the $CrPS_4$ with two different magnetic structures (antiferromagnetic and ferromagnetic) was carried out using the Vienna Ab

initio Simulation Package (VASP)[51,52]. In the calculation, the Perdew-Burke-Ernzerhof (PBE) functional is employed to describe the exchange and correlation[53]. The van der Waals density functional with optimized Becke88 parameterizations (vdW-DF-optB88) functional is used to account for the interlayer van der Waals interactions in bulk $CrPS_4$[54-57]. An on-site Coulomb repulsion term U=2 eV was used for Cr 3d electrons in the calculation to give a proper bandgap[24]. The calculated band structures and density of states (DOS) are given in supplementary FIG. S6. The band structures indicate that both antiferromagnetic $CrPS_4$ and the ferromagnetic $CrPS_4$ are direct band semiconductors, with top of the valence band and bottom of the conduction band occur at the same value of momentum. The DOS indicates that the antiferromagnetic state has a larger bandgap (1.047 eV) than the ferromagnetic state (0.977 eV). This explains the negative δMR_{xx} observed in the heterostructure at $T<T_N$.

It is noted that δMR_{xx} does not show any SF-related signal in the $CrPS_4$/Pd device, which is different from the previously reported CrI_3/Pt device[47], where R_{xx} shows a signal from current induced SF. We conjecture two reasons for this. The first reason is that although $CrPS_4$ has a quite similar magnetic structure to CrI_3, the spin dynamics in these two systems are quite different, because here the bulk $CrPS_4$ properties are detected while a surface SF is detected in CrI_3 as there is not an intrinsic bulk SF transition in CrI_3. Thus, our result represents the first direct electrical readout of the intrinsic (solely triggered by the external magnetic field) SF of a vdW antiferromagnet using transport measurement. Another possible reason is that the SF signal is overwhelmed by the bulk $CrPS_4$ resistance change induced by the magnetic field, and thus cannot be detected, while in the R_{xy} signal, the interference from the bulk $CrPS_4$ signal will be much smaller.

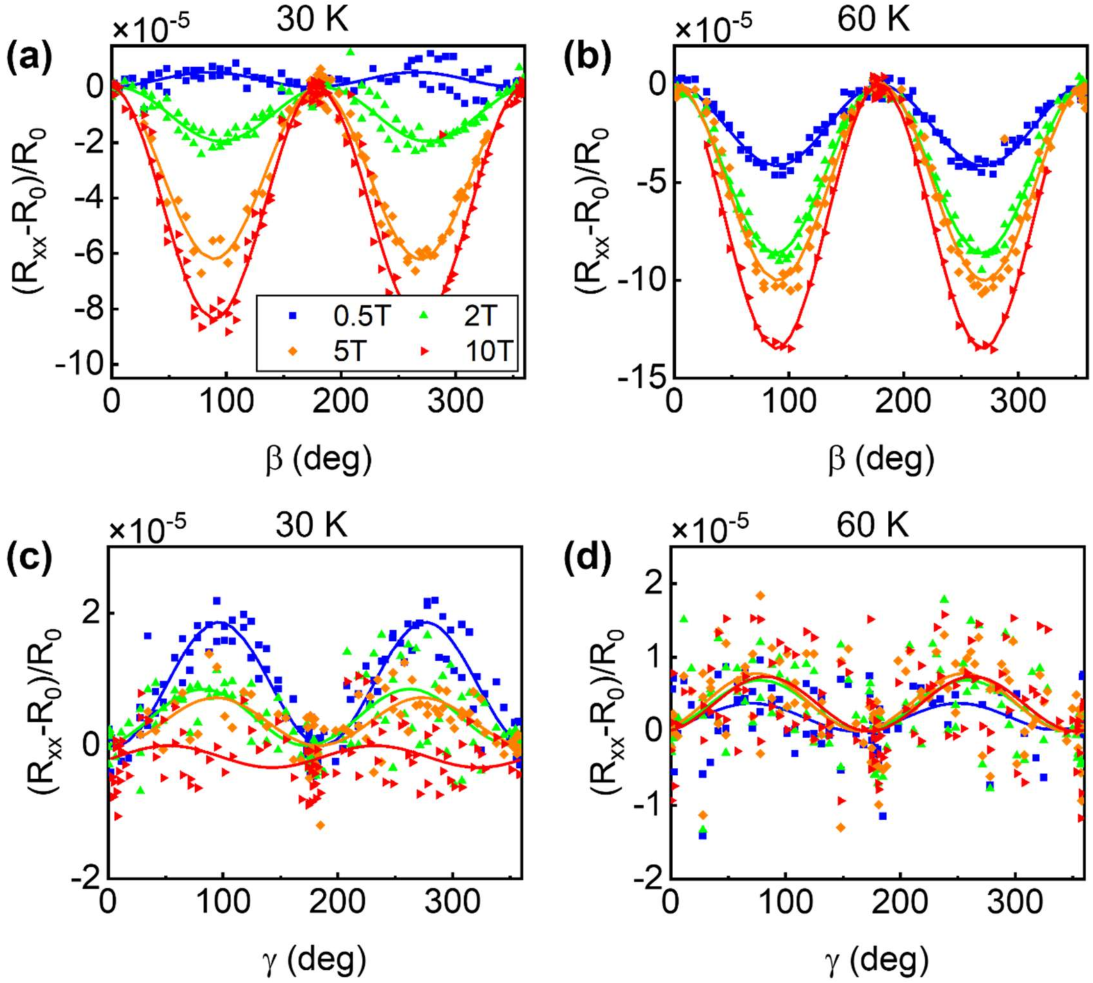

FIG. 4. Spin-Hall magnetoresistance in the $CrPS_4$/Pd heterostructure. (a) and (b) show the β angle dependence at 30 K and 60 K, respectively. (c) and (d) show the γ angle dependence at 30 K and 60 K, respectively. The scatter indicates the experimental results, and the solid curves indicate the best-fitting of the experimental results.

Finally, we probe the angular variation of the signals by rotating the magnetic field to understand the possible antiferromagnetic and the ferromagnetic-like signals and the SMR and the AMR origin better. The angular dependence of the resistance of the $CrPS_4$/Pd device are measured at two different temperatures, 30 K (below T_N) and 60 K (above T_N). In the SMR scenario, the MR depends on the angle between the nonequilibrium spin accumulation $\boldsymbol{\sigma}$ in the heavy metal layer and the magnetization $\boldsymbol{M}$ of the magnetic layer. In contrast, the AMR depends on the angle between the current

$\boldsymbol{J}$ and the magnetization $\boldsymbol{M}$.

FIG. 4(a) and 4(b) show the field dependence of $\delta R_{xx}(\beta)$ at 30 K. Here, β is the angle between the field and the y axis when the field is rotated in the yz plane, which is zero when the field is parallel to y. Since $\boldsymbol{M}$ is always perpendicular to $\boldsymbol{J}$ in this rotation plane, the magnetoresistance, if detected, should result from SMR only. It is found that the $\delta R_{xx}(\beta)$ shows maxima at 90° and 270° when the field is about 0.5 T. However, it shows minima at the same angles at higher fields. While the latter behavior can be well explained with the SMR scenario, i.e. the R_{xx} is minimum when $\boldsymbol{M}//\boldsymbol{\sigma}$, the anomalous behavior at 0.5 T can be ascribed to the SF. This behavior disappears at a higher temperature (T=60 K), as shown in FIG. 4(b), where a larger SMR effect is observed, indicating possibly a higher interfacial ferromagnetic magnetization, coming from the top $CrPS_4$ layer in contact with the heavy metal. This is in good agreement with the larger R_{xy} that we observe at a higher temperature.

FIG. 4(c) and 4(d) show the field dependence of $\delta R_{xx}(\gamma)$ at 30 K and 60 K, respectively. Here, γ is defined as the angle between the field and x axis when field rotates in the x-z plane, which is zero when the field is along the z axis. Since $\boldsymbol{M}$ is always perpendicular to $\boldsymbol{\sigma}$ in this rotation plane, the magnetoresistance should be a result of only AMR. It is found that no obvious AMR was visible at 60 K, however, a weak AMR signal was observed at 0.5 T and 30 K. This can be ascribed to the AMR effect of the $CrPS_4$ due to the electronic band structure modification by the magnetic field, which is more pronounced at temperatures below T_N.

Conclusions

In conclusion, we have determined the magnetic transport properties of the $CrPS_4$/(Pd, Pt) heterostructures. The SF can be unambiguously detected in both systems, indicating the spin-transparent interfaces are formed in those vdW/heavy metal heterostructures. Furthermore, an anomalous Hall effect observed at up to room temperature possibly indicates enhanced magnetic ordering temperature due to the large spin-orbit coupling at the interface, which suggests potentially a route to achieve room temperature 2D magnetic ordering using a proximity effect. This is of key importance as it would enable a range of device applications in memory or logic that have been suggested to benefit from the enhanced properties antiferromagnetic systems and that typically require operation at room temperature. A negative magnetoresistance observed below T_N is explained by the magnetic field modified electronic band structure of the $CrPS_4$. The total magnetoresistance is a superposition of the SMR and the magnetoresistance from $CrPS_4$. It needs to be pointed out that there are still some issues that is not fully clear at this stage and need to be studied further, e.g., the origin of the AHE at temperatures higher than T_N and the origin of the THE-like feature in the R_{xy} signal. XMCD and XMCD-PEEM measurements could be carried out to detect the possible magnetic ordering and the topological magnetic structure at above T_N. However, at this stage we prefer to leave them as open problems. Nevertheless, our results demonstrate the electrical detection of two-dimensional magnetism and thus provide a new route to realize two-dimensional magnetism above room temperature, highlighting the potential of vdW magnets for spintronic device applications.

Acknowledgements

We acknowledge funding from Deutsche Forschungsgemeinschaft (DFG, German Research Foundation) – Spin+X TRR 173 – 268565370 (Projects No. A01 and No. B02), DFG Project No. 358671374, Graduate School of Excellence Materials Science in Mainz (MAINZ) GSC 266, the MaHoJeRo (DAAD Spintronics network, Projects No.57334897 and No. 57524834), the Research Council of Norway (Centre for Quantum Spintronics - QuSpin No. 262633), National Key Research and Development Program of China (Grants No. 2016YFB0700901, No. 2017YFA0206303, and No.

2017YFA0403701), and National Natural Science Foundation of China (Grants No. 51731001, No. 11675006, No.11805006, No. 11975035, No. 12104052 and No. 211012180393).

References

[1] T. Jungwirth, J. Wunderlich, and K. Olejník, Spin Hall effect devices, Nat. Mater. **11**, 382 (2012).

[2] J. Han, A. Richardella, S. A. Siddiqui, J. Finley, N. Samarth, and L. Liu, Room-Temperature Spin-Orbit Torque Switching Induced by a Topological Insulator, Phys. Rev. Lett. **119**, 077702 (2017).

[3] Y. Fan, P. Upadhyaya, X. Kou, M. Lang, S. Takei, Z. Wang, J. Tang, L. He, L.-T. Chang, M. Montazeri *et al.*, Magnetization switching through giant spin–orbit torque in a magnetically doped topological insulator heterostructure, Nat. Mater. **13**, 699 (2014).

[4] J. Sinova, S. O. Valenzuela, J. Wunderlich, C. H. Back, and T. Jungwirth, Spin Hall effects, Rev. Mod. Phys. **87**, 1213 (2015).

[5] H. Nakayama, M. Althammer, Y. T. Chen, K. Uchida, Y. Kajiwara, D. Kikuchi, T. Ohtani, S. Geprags, M. Opel, S. Takahashi *et al.*, Spin Hall magnetoresistance induced by a nonequilibrium proximity effect, Phys. Rev. Lett. **110**, 206601 (2013).

[6] K. S. Burch, D. Mandrus, and J. G. Park, Magnetism in two-dimensional van der Waals materials, Nature **563**, 47 (2018).

[7] Y. Deng, Y. Yu, Y. Song, J. Zhang, N. Z. Wang, Z. Sun, Y. Yi, Y. Z. Wu, S. Wu, J. Zhu *et al.*, Gate-tunable room-temperature ferromagnetism in two-dimensional Fe_3GeTe_2, Nature **563**, 94 (2018).

[8] T. Song, Z. Fei, M. Yankowitz, Z. Lin, Q. Jiang, K. Hwangbo, Q. Zhang, B. Sun, T. Taniguchi, K. Watanabe *et al.*, Switching 2D magnetic states via pressure tuning of layer stacking, Nat. Mater. **18**, 1298 (2019).

[9] C. Gong, L. Li, Z. Li, H. Ji, A. Stern, Y. Xia, T. Cao, W. Bao, C. Wang, Y. Wang *et*

al., Discovery of intrinsic ferromagnetism in two-dimensional van der Waals crystals, Nature **546**, 265 (2017).

[10] S. Ding, Z. Liang, J. Yang, C. Yun, P. Zhang, Z. Li, M. Xue, Z. Liu, G. Tian, F. Liu *et al.*, Ferromagnetism in two-dimensional Fe_3GeTe_2; Tunability by hydrostatic pressure, Phys. Rev. B **103**, 094429 (2021).

[11] M. Lohmann, T. Su, B. Niu, Y. Hou, M. Alghamdi, M. Aldosary, W. Xing, J. Zhong, S. Jia, W. Han *et al.*, Probing Magnetism in Insulating $Cr_2Ge_2Te_6$ by Induced Anomalous Hall Effect in Pt, Nano Lett. **19**, 2397 (2019).

[12] K. Dolui, M. D. Petrovic, K. Zollner, P. Plechac, J. Fabian, and B. K. Nikolic, Proximity Spin-Orbit Torque on a Two-Dimensional Magnet within van der Waals Heterostructure: Current-Driven Antiferromagnet-to-Ferromagnet Reversible Nonequilibrium Phase Transition in Bilayer CrI_3, Nano Lett. **20**, 2288 (2020).

[13] N. D. Mermin and H. Wagner, Absence of Ferromagnetism or Antiferromagnetism in One- or Two-Dimensional Isotropic Heisenberg Models, Phys. Rev. Lett. **17**, 1133 (1966).

[14] T. Song, X. Cai, M. W. Tu, X. Zhang, B. Huang, N. P. Wilson, K. L. Seyler, L. Zhu, T. Taniguchi, K. Watanabe *et al.*, Giant tunneling magnetoresistance in spin-filter van der Waals heterostructures, Science **360**, 1214 (2018).

[15] T. Song, M. W. Tu, C. Carnahan, X. Cai, T. Taniguchi, K. Watanabe, M. A. Mcguire, D. H. Cobden, D. Xiao, W. Yao *et al.*, Voltage Control of a van der Waals Spin-Filter Magnetic Tunnel Junction, Nano Lett. **19**, 915 (2019).

[16] W. Y. Xing, L. Y. Qiu, X. R. Wang, Y. Y. Yao, Y. Ma, R. R. Cai, S. Jia, X. C. Xie, and W. Han, Magnon Transport in Quasi-Two-Dimensional van der Waals Antiferromagnets, Phys. Rev. X **9**, 011026 (2019).

[17] G. Chen, S. Qi, J. Liu, D. Chen, J. Wang, S. Yan, Y. Zhang, S. Cao, M. Lu, S. Tian *et al.*, Electrically switchable van der Waals magnon valves, Nat. Commun. **12**, 6279 (2021).

[18] S. Jiang, L. Li, Z. Wang, K. F. Mak, and J. Shan, Controlling magnetism in 2D CrI_3 by electrostatic doping, Nat. Nanotechnol. **13**, 549 (2018).

[19] S. Jiang, J. Shan, and K. F. Mak, Electric-field switching of two-dimensional van der Waals magnets, Nat. Mater. **17**, 406 (2018).

[20] B. Huang, G. Clark, E. Navarro-Moratalla, D. R. Klein, R. Cheng, K. L. Seyler, D. Zhong, E. Schmidgall, M. A. Mcguire, D. H. Cobden *et al.*, Layer-dependent ferromagnetism in a van der Waals crystal down to the monolayer limit, Nature **546**, 270 (2017).

[21] L. Thiel, Z. Wang, M. A. Tschudin, D. Rohner, I. Gutierrez-Lezama, N. Ubrig, M. Gibertini, E. Giannini, A. F. Morpurgo, and P. Maletinsky, Probing magnetism in 2D materials at the nanoscale with single-spin microscopy, Science **364**, 973 (2019).

[22] S. Calder, A. V. Haglund, Y. Liu, D. M. Pajerowski, H. B. Cao, T. J. Williams, V. O. Garlea, and D. Mandrus, Magnetic structure and exchange interactions in the layered semiconductor $CrPS_4$, Phys. Rev. B **102**, 024408 (2020).

[23] Y. Peng, S. Ding, M. Cheng, Q. Hu, J. Yang, F. Wang, M. Xue, Z. Liu, Z. Lin, M. Avdeev *et al.*, Magnetic Structure and Metamagnetic Transitions in the van der Waals Antiferromagnet $CrPS_4$, Adv. Mater. **32**, e2001200 (2020).

[24] H. L. L. Zhuang and J. Zhou, Density functional theory study of bulk and single-layer magnetic semiconductor $CrPS_4$, Phys. Rev. B **94**, 195307 (2016).

[25] J. Son, S. Son, P. Park, M. Kim, Z. Tao, J. Oh, T. Lee, S. Lee, J. Kim, K. Zhang *et al.*, Air-Stable and Layer-Dependent Ferromagnetism in Atomically Thin van der Waals $CrPS_4$, ACS Nano **15**, 16904 (2021).

[26] Q. L. Pei, X. Luo, G. T. Lin, J. Y. Song, L. Hu, Y. M. Zou, L. Yu, W. Tong, W. H. Song, W. J. Lu *et al.*, Spin dynamics, electronic, and thermal transport properties of two-dimensional $CrPS_4$ single crystal, J. Appl. Phys. **119**, 043902 (2016).

[27] Y. Tserkovnyak and M. Klaui, Exploiting Coherence in Nonlinear Spin-Superfluid Transport, Phys. Rev. Lett. **119**, 187705 (2017).

[28] A. Qaiumzadeh, H. Skarsvag, C. Holmqvist, and A. Brataas, Spin Superfluidity in Biaxial Antiferromagnetic Insulators, Phys. Rev. Lett. **118**, 137201 (2017).

[29] R. Lebrun, A. Ross, S. A. Bender, A. Qaiumzadeh, L. Baldrati, J. Cramer, A. Brataas, R. A. Duine, and M. Klaui, Tunable long-distance spin transport in a crystalline

antiferromagnetic iron oxide, Nature **561**, 222 (2018).

[30]F. L. A. Machado, P. R. T. Ribeiro, J. Holanda, R. L. Rodriguez-Suarez, A. Azevedo, and S. M. Rezende, Spin-flop transition in the easy-plane antiferromagnet nickel oxide, Phys. Rev. B **95**, 104418 (2017).

[31]S. Seki, T. Ideue, M. Kubota, Y. Kozuka, R. Takagi, M. Nakamura, Y. Kaneko, M. Kawasaki, and Y. Tokura, Thermal Generation of Spin Current in an Antiferromagnet, Phys. Rev. Lett. **115**, 266601 (2015).

[32]J. Lee, T. Y. Ko, J. H. Kim, H. Bark, B. Kang, S.-G. Jung, T. Park, Z. Lee, S. Ryu, and C. Lee, Structural and Optical Properties of Single- and Few-Layer Magnetic Semiconductor $CrPS_4$, ACS Nano **11**, 10935 (2017).

[33]See Supplemental Material at [URL will be inserted by publisher] for the Raman spectroscopy of the $CrPS_4$ flake, processing of the raw R_{xy} signal, subtracting the R_{xx} signal of Pd from the signal of $CrPS_4$/Pd, R_{xy} signal obtained from the $CrPS_4$/Pd device with H//x and H//y, and DFT calculated electronic structures of antiferromagnetic and ferromagnetic $CrPS_4$.

[34]H. J. Lee, E. Helgren, and F. Hellman, Gate-controlled magnetic properties of the magnetic semiconductor (Zn,Co)O, Appl. Phys. Lett. **94**, 212106 (2009).

[35]D. H. Wei, Y. Niimi, B. Gu, T. Ziman, S. Maekawa, and Y. Otani, The spin Hall effect as a probe of nonlinear spin fluctuations, Nat. Commun. **3**, 1058 (2012).

[36]H. Yang, A. Thiaville, S. Rohart, A. Fert, and M. Chshiev, Anatomy of Dzyaloshinskii-Moriya Interaction at Co/Pt Interfaces, Phys. Rev. Lett. **115**, 267210 (2015).

[37]W. X. Zhu, C. Song, L. Han, H. Bai, Q. Wang, S. Q. Yin, L. Huang, T. J. Chen, and F. Pan, Interface-Enhanced Ferromagnetism with Long-Distance Effect in van der Waals Semiconductor, Adv. Funct. Mater. **32**, 2108953 (2022).

[38]D. Gu, S. K. Dey, and P. Majhi, Effective work function of Pt, Pd, and Re on atomic layer deposited HfO_2, Appl. Phys. Lett. **89**, 082907 (2006).

[39]P. Bruno, V. K. Dugaev, and M. Taillefumier, Topological Hall effect and Berry phase in magnetic nanostructures, Phys. Rev. Lett. **93**, 096806 (2004).

[40] P. Swekis, A. Markou, D. Kriegner, J. Gayles, R. Schlitz, W. Schnelle, S. T. B. Goennenwein, and C. Felser, Topological Hall effect in thin films of Mn1.5PtSn, Phys. Rev. Mater. **3**, 013001 (2019).
[41] N. Kanazawa, Y. Onose, T. Arima, D. Okuyama, K. Ohoyama, S. Wakimoto, K. Kakurai, S. Ishiwata, and Y. Tokura, Large topological Hall effect in a short-period helimagnet MnGe, Phys. Rev. Lett. **106**, 156603 (2011).
[42] T. Kurumaji, T. Nakajima, M. Hirschberger, A. Kikkawa, Y. Yamasaki, H. Sagayama, H. Nakao, Y. Taguchi, T. H. Arima, and Y. Tokura, Skyrmion lattice with a giant topological Hall effect in a frustrated triangular-lattice magnet, Science **365**, 914 (2019).
[43] Q. M. Shao, Y. W. Liu, G. Q. Yu, S. K. Kim, X. Y. Che, C. Tang, Q. L. He, Y. Tserkovnyak, J. Shit, and K. L. Wang, Topological Hall effect at above room temperature in heterostructures composed of a magnetic insulator and a heavy metal, Nat. Electron. **2**, 182 (2019).
[44] Y. Cheng, S. Yu, M. Zhu, J. Hwang, and F. Yang, Evidence of the Topological Hall Effect in Pt/Antiferromagnetic Insulator Bilayers, Phys. Rev. Lett. **123**, 237206 (2019).
[45] Y. K. Park, D. Y. Kim, J. S. Kim, Y. S. Nam, M. H. Park, H. C. Choi, B. C. Min, and S. B. Choe, Experimental observation of the correlation between the interfacial Dzyaloshinskii-Moriya interaction and work function in metallic magnetic trilayers, NPG Asia Mater. **10**, 995 (2018).
[46] L. Baldrati, C. Schmitt, O. Gomonay, R. Lebrun, R. Ramos, E. Saitoh, J. Sinova, and M. Klaui, Efficient Spin Torques in Antiferromagnetic CoO/Pt Quantified by Comparing Field- and Current-Induced Switching, Phys. Rev. Lett. **125**, 077201 (2020).
[47] T. Su, M. Lohmann, J. Li, Y. Xu, B. Niu, M. Alghamdi, H. Zhou, Y. Cui, R. Cheng, T. Taniguchi *et al.*, Current-induced CrI_3 surface spin-flop transition probed by proximity magnetoresistance in Pt, 2D Materials **7**, 045006 (2020).
[48] A. Ross, R. Lebrun, C. Ulloa, D. A. Grave, A. Kay, L. Baldrati, F. Kronast, S. Valencia, A. Rothschild, and M. Klaui, Structural sensitivity of the spin Hall magnetoresistance in antiferromagnetic thin films, Phys. Rev. B **102**, 094415 (2020).

[49] Y. T. Chen, S. Takahashi, H. Nakayama, M. Althammer, S. T. B. Goennenwein, E. Saitoh, and G. E. W. Bauer, Theory of spin Hall magnetoresistance, Phys. Rev. B **87**, 144411 (2013).

[50] M. I. Dyakonov, Magnetoresistance due to edge spin accumulation, Phys. Rev. Lett. **99**, 126601 (2007).

[51] G. Kresse and J. Hafner, Ab initio molecular dynamics for liquid metals, Phys. Rev. B **47**, 558 (1993).

[52] G. Kresse and J. Furthmuller, Efficient iterative schemes for ab initio total-energy calculations using a plane-wave basis set, Phys. Rev. B **54**, 11169 (1996).

[53] J. P. Perdew, K. Burke, and M. Ernzerhof, Generalized Gradient Approximation Made Simple, Phys. Rev. Lett. **77**, 3865 (1996).

[54] M. Dion, H. Rydberg, E. Schroder, D. C. Langreth, and B. I. Lundqvist, van der Waals density functional for general geometries, Phys. Rev. Lett. **92**, 246401 (2004).

[55] G. Roman-Perez and J. M. Soler, Efficient implementation of a van der Waals density functional: application to double-wall carbon nanotubes, Phys. Rev. Lett. **103**, 096102 (2009).

[56] T. Thonhauser, V. R. Cooper, S. Li, A. Puzder, P. Hyldgaard, and D. C. Langreth, Van der Waals density functional: Self-consistent potential and the nature of the van der Waals bond, Phys. Rev. B **76**, 125112 (2007).

[57] J. Klimes, D. R. Bowler, and A. Michaelides, Chemical accuracy for the van der Waals density functional, J. Phys.: Condens. Matter **22**, 022201 (2010).